ELSEVIER

Contents lists available at ScienceDirect

Chemical Engineering Journal

journal homepage: www.elsevier.com/locate/cej





3D-Printed functionally graded thermoelectric materials for enhanced power generation

Hyunjin Han^{a,1}, Seong Eun Yang^{a,1}, Jungsoo Lee^a, Keonkuk Kim^a, Changhyeon Nam^b, Seungki Jo^c, So-Hyeon Lee^d, Ju-Young Kim^d, Sangjoon Ahn^b, Jae Sung Son^{a,*}

- a Department of Chemical Engineering, Pohang University of Science and Technology (POSTECH), RIST 3-3246, Pohang, Gyeongsangbuk-do 37673., Republic of Korea
- b Department of Nuclear Engineering, Ulsan National Institute of Science and Technology (UNIST), Ulsan 44919, Republic of Korea
- ^c Nanomaterials Research Division, Korea Institute of Materials Science (KIMS), 797 Changwon-daero, Changwon-si 51508, Gyeongnam, Republic of Korea
- d Department for Materials Science and Engineering, Ulsan National Institute of Science and Technology (UNIST), Ulsan 44919, Republic of Korea

ARTICLE INFO

Keywords: Functionally graded material Thermoelectric generator 3D printing Viscoelastic ink Bi₂Te₃

ABSTRACT

Functionally graded materials (FGMs) are heterogeneous, with compositions that vary spatially with respect to their dopant concentrations and structures. FGMs are designed to exhibit the desired properties and functionalities for various target applications. Recently, 3D printing has emerged as a promising method for fabricating FGMs with complex customized geometries and precise distributions of materials. However, the use of 3D printing to fabricate FGMs is generally limited to producing structural materials, and their application to energy and electronic materials remains relatively rare. Thermoelectric power generation is regarded as a unique solution to recover waste heat; however, the strong temperature dependence of suitably efficient materials restricts their widespread application. Herein, we report a sequential 3D printing method for fabricating n-type Bi₂Te_{2.7}Se_{0.3} thermoelectric materials with electronic dopant and structural void gradients. The formulation of Na-doped Bi₂Te_{2.7}Se_{0.3} particle colloid inks with the desired viscoelasiticity for 3D printing enabled the fabrication of materials with complex architectures and a precision of 150 µm. These materials incorporated atomic doping and macroscopic void gradients. The thermoelectric peak temperatures of the printed materials varied from room temperature to 450 K, depending on the doping concentration. The graded thermoelectric materials were designed to have a wide operable temperature window and was fabricated by 3D printing, thereby enabling the fabricated devices to deliver enhanced power-generating performance compared with that of devices based on the homogeneous material. The proposed method enables rapid and cost-effective production of functionally graded thermoelectric materials with applications in energy and electronic devices.

1. Introduction

Functionally graded materials (FGMs) represent a class of advanced materials that are designed to have a gradient in their composition, microstructure, or porosity along single or multiple spatial directions. These gradients result in a continuous variation in properties and functions over the volume of these materials [1–3]. Various functional effects can be created by fabricating FGMs, which have found application in diverse fields such as electrical or electronic [4–9], biomedical

[10–13], aerospace [14–16], automotive [17,18], defense [19], marine [20], optoelectronic [21,22], and energy devices [23–28]. Various liquid- and solid-phase methods have been proposed for producing bulk FGMs [29]. For instance, the centrifugal casting process involves adding a second phase to a molten metal and applying a centrifugal force to create a gradient of the second phase in the bulk composite. Another solid-state powder metallurgy method involves stacking powders according to a predesigned spatial distribution, followed by sintering. However, precise control and optimization of the gradient in FGMs

Abbreviations: FGMs, functionally graded materials; TE, thermoelectric; TEG, thermoelectric generator; ZT, thermoelectric figure of merit; FGTEMs, functionally graded thermoelectric materials; CAD, computer-aided design model; ChaM, chalcogenidometallate; XRD, X-ray diffraction; SEM, scanning electron microscopy; EDS, energy-dispersive X-ray spectroscopy; OM, optical microscopy.

^{*} Corresponding author.

E-mail address: sonjs@postech.ac.kr (J. Sung Son).

¹ These authors contributed equally to this work.

remains a challenge via both the liquid- and solid-phase approaches [30].

Recently, 3D printing has emerged as a method for manufacturing FGMs with high-precision gradient profiles because of its nature, which builds materials or components in a layer-by-layer manner [1,31,32]. Moreover, 3D printing can simplify the process of manufacturing FGM-based components because it can directly produce FGMs with customized complex geometries without requiring post-machining of the product. To date, studies on FGMs produced using 3D printing have been primarily aimed at enhancing the mechanical properties of metallic structural materials [33]. However, reports on the synthesis and fabrication of other functional materials, such as electronic and energy materials, as FGMs via 3D printing remain relatively scarce. Considering the widespread application of FGMs in the energy and electronic sectors, including as thermoelectric, dielectric, and piezoelectric materials [34,35], their fabrication via 3D printing is worthy of investigation.

Thermoelectric (TE) power generators have been attracting considerable interest as devices for recovering renewable energy because they can directly generate electricity from waste heat without causing any environmental pollution [36-38]. The efficiency of TE materials is determined by a figure of merit (ZT), which is evaluated using the equation $ZT=S^2\sigma T/\kappa$, where S, σ , κ , and T are the Seebeck coefficient, electrical conductivity, thermal conductivity, and absolute temperature, respectively. TE properties are strongly dependent on temperature, for example, the ZT of Bi₂Te₃-based TE materials reaches a maximum value at approximately room temperature and subsequently decreases rapidly with increasing temperature. This means that a TE generator (TEG) generally does not operate in the temperature range in which its ZT is maximum [39-41]. One approach to addressing this issue is segmenting multiple materials or cascading multiple devices with different ranges of best-service temperatures [42-46]. This would enable each segment of the device to function in a temperature range in which the other segment (s) do not contribute to the conversion process, thereby contributing to the overall power generation efficiency. Despite this being an ideal theoretical concept, a critical problem arising from this strategy is the unavoidable thermal and electrical losses at the interfaces between multiple segments or devices. Enhancement of the power generated by these systems, therefore, requires meticulous optimization of the material compatibility and/or engineering in metallization and bonding [47–50]. Another prominent strategy is achieving a property gradient in TE materials, mainly in terms of the carrier concentration, which enables the peak ZT temperature of TE semiconductors to be adjusted by controlling the bipolar effect at elevated temperatures [51-54]. TE materials with a carrier concentration gradient have been fabricated via traditional metallurgical methods, such as that of Bridgman and Czochralski, or hot-pressing methods; however, the high-precision control of gradation remains difficult [55-59].

Bi₂Te₃-based materials are workhorse n-type TE materials operable at room temperature, and their properties resulting from doping are well-established [40,60-71]. In this paper, we report a sequential 3D printing method for achieving doping concentration and structural gradients in n-type $Bi_2Te_{2.7}Se_{0.3}$ TE materials. We precisely controlled the concentration of the Na dopant in the formulated Bi₂Te_{2.7}Se_{0.3} inks by tailoring the rheological properties by adding molecular anionic complexes of Sb₂Te₄²⁻ to induce an electroviscous effect to improve the viscoelasticity. These inks were sequentially deposited in a layer-bylayer manner by employing the extrusion 3D printing process to create TE materials with a doping gradient or graded structural voids with a precision of 150 μm in the thickness direction. These FGMs have the potential to exhibit synergistic functional properties via the combined gradient of electronic and structural characteristics. The TE properties of the 3D-printed Na-doped TE materials, including the variation in the maximum ZT in the range from room temperature to 450 K, clearly depend on the doping concentration. Based on these temperature dependences, a TEG consisting of a multiply graded n-type Bi₂Te_{2.7}Se_{0.3} leg, doped with increasing concentrations of Na ions in a stepwise

manner, combined with a p-type $Bi_ySb_{2\cdot y}Te_3$ leg, was designed and evaluated in comparison with a TEG consisting of homogeneous materials. The proposed 3D printing process can be used to fabricate efficient functionally graded TE materials (FGTEMs) and devices.

2. Experimental section

2.1. Materials

Bi, Sb, and Te granules (>99.999 %) were purchased from Thermoelectric Total Solution, and Na (>99.9 %), ethanethiol (>97 %), ethylenediamine (>99.5 %), acetonitrile (>99.8 %), and glycerol (>99.5 %) were purchased from Aldrich Chemical Co. Se (>99.999 %) was purchased from Thermo Fisher Scientific.

2.2. Synthesis of Bi₂Te_{2.7}Se_{0.3} based inks doped with x wt% Na

The Bi, Sb, and Te granules were ball-milled using a SPEX 8000 M Mixer/Mill to obtain fine powders. Stainless-steel balls, comprising two balls with a diameter of 12.7 mm and four balls with a diameter of 6.35 mm, were employed for a milling duration of 30 min. TE powders with a stoichiometric composition of Bi₂Te_{2.7}Se_{0.3} with Na doping concentrations of 0-0.25 wt%, were synthesized via mechanical alloying using high-energy ball milling (Fritsch Monomill, Pulverisette, Germany) at 450 rpm for 12 h. A zirconia (ZrO2) jar with a volume of 80 mL and zirconia grinding balls, each with a diameter of 5 mm, were used and a 5:1 wt ratio of the balls to the powder was maintained. The $Sb_2Te_4^2$ additive was synthesized by mixing 0.64 g of Sb powder and 1.36 g of Te powder in a co-solvent consisting of 4 mL of ethanethiol and 16 mL of ethylenediamine at room temperature in a glove box under N2 atmosphere. The mixture was stirred for more than 24 h using a magnetic stirrer. Subsequently, acetonitrile was added to the mixed solution at an 8:1 vol ratio, whereupon the Sb₂Te₄²⁻ powder was precipitated via centrifugation at 7,500 rpm for 10 min, followed by vacuum drying for 1 h. To formulate the viscoelastic TE ink, the TE powder and Sb₂Te₄² were combined with glycerol and stirred using a planetary centrifugal mixer (ARM-100, Thinky) for 1.5 h.

2.3. 3D printing of FGTEMs

The formulated TE inks were used for printing by employing an extrusion-based 3D printer equipped with a nozzle connected to an ink reservoir, a pressure controller, a compressor unit, and a three-axis stage with a stepper motor. The TE inks were loaded in a printing barrel with a volume of 5 mL (Saejong), and they were released with resolution of 200-1000 µm. Using a computer-aided design by Blender, SolidWorks, and Ultimaker Cura, we deposited the TE inks on a graphite substrate. The extrusion pressure was adjusted using a dispensing controller (Saejong). The FGTEMs were sequentially printed using TE inks containing $Bi_2Te_{2.7}Se_{0.3}/Na x$ wt% (x = 0.175, 0.1, and 0) and $Bi_vSb_{2-v}Te_3$ (y = 0.55, 0.5, and 0.35). The as-printed n-type TE materials and the FGTEMs were dried at 403 K on a hot plate for 24 h and then sintered at 783 K for 3 h in a box furnace in a glove box filled with N2 gas. The asprinted p-type FGTEM was dried at 423 K on a hot plate for 24 h and then sintered at 723 K for 3 h in a tube furnace in an atmosphere containing 4 % H₂ and 96 % Ar.

2.4. Characterization of materials

An oscillating rheometer (Haake MARS III, Thermo Scientific) was used to analyze the rheology of the Na-doped $\rm Bi_2Te_{2.7}Se_{0.3}$ TE inks. During the frequency sweep tests, the stress was maintained at 1 Pa, whereas the stress sweep assessments were performed at a frequency of 1 rad s $^{-1}$ to vary the stress in the range 0.005–300 Pa.

X-ray diffraction (XRD) analysis was conducted using a high-power X-ray diffractometer (Rigaku) with a Cu-rotating anode X-ray source

operating at 20 kV and 10 mA at the 2θ range from 10° to 70° and scan speed of 4° min $^{-1}$. The microstructure of $Bi_2Te_{2.7}Se_{0.3}$ with Na-doping concentrations of 0–0.2 wt% was examined using scanning electron microscopy (SU7000 FE-SEM, Hitachi High-Tech Corporation) at an accelerating voltage of 15 kV. Doping gradient in the printed sample was evaluated via energy-dispersive spectroscopy (EDS). Optical microscopy (OM) images of the as-printed filaments were acquired using an Olympus BX51M instrument. The compressive tests were performed using universal testing systems (5948 MicroTester, Instron) with a strain rate of $1\times 10^{-3}~\text{s}^{-1}$.

Using a thermal analyzer (SBA458 Nemesis, NETZSCH, Germany), the electrical conductivity and Seebeck coefficient were measured in the temperature range 300-525 K under Ar. The equation $\kappa=\alpha c\rho$, where ρ is the density, α is the specific heat capacity, and c is the thermal diffusivity, was used to calculate the thermal conductivity (κ). The thermal diffusivity was evaluated using a laser flash analyzer (LFA-457, NETZSCH, Germany) in the temperature range 300-525 K. The dimensions and measured weights of the polished sample were used to calculate the relative densities. Hall measurements (HMS-5000, ECO-PIA) were conducted to determine the carrier concentrations and mobilities of Na-doped Bi₂Te_{2.7}Se_{0.3} at room temperature.

2.5. Numerical simulation of TEG

A three-dimensional finite element analysis (FEA) was developed using COMSOL Multiphysics, a commercial software, to calculate the temperature distribution and the electrical properties such as output voltage, resistance, and output power in the TEG at steady-state. A model containing electrodes and TE legs with the same dimensions as those used in the experiment was used for the calculations. The material properties of the TE leg measured in previous experimental section were interpolated using the cubic spline to simulate. The electrical contact resistance between TE leg and electrodes was applied using experimentally measured values. As boundary conditions, the hot-side temperature was increased from 350 K to 525 K and the cold-side temperature was maintained at 300 K. Similar to the vacuum condition, the lateral sides were applied adiabatic condition. The cold-side electrode of n-type TE leg was electrically grounded.

2.6. Measurement of the power output of the FGTEM module and homogeneous material TEG

Copper electrodes with a length of 0.5 mm were used in the FGTEM module and homogeneous material TEG. The p-type FGTEM (5 \times 5 \times 5 [mm³]) and n-type FGTEM (5.23 mm \times 5.23 mm \times 5 mm) were soldered with copper electrodes using Sn/Ag/Cu solder at 623 K. In the case of the homogeneous material TEG, p-type $Bi_{0.35}Sb_{1.65}Te_3$ (5 mm \times 5 mm \times 5 mm) and n-type $Bi_2Te_{2.7}Se_{0.3}$ doped with 0.175 wt% Na (5.23 mm \times $5.23 \text{ mm} \times 5 \text{ mm}$) were used. All measurements were conducted under vacuum. A ceramic heater was used as the heat source, and a watercirculating cooler for heat dissipation was used to control the temperatures on the hot and cold sides. A thermal pad with a thickness of 0.5 mm (Thermalright, Valor Odin) was used to insulate the TEG and maintain contact with the heater and cooler. The FGTEM module and homogeneous material TEG were connected to the feedthrough of a vacuum chamber (<10⁻² torr), which was connected to a Keithley 2400 to measure the generated voltage, resistance, and power supply of the heater. The hot- and cold-side temperatures were recorded by attaching thermocouples (T-type) between the electrode and TE leg.

2.7. Calculation of optimal TE leg height and areal ratio

The TE properties of the n-type materials obtained were fitted as a function of temperature. The calculations revealed that $\rm Bi_2Te_{2.7}Se_{0.3}$ doped with 0, 0.1, and 0.175 wt% Na had the highest ZT in the temperature ranges of 450.18–525 K, 390.63–450.18 K, and 300–390.63 K,

respectively. As indicated by the calculations by Yang et al. [49], p-type $Bi_vSb_{2-v}Te_3$ (y = 0.35, 0.5, and 0.55) materials have the highest ZT in the temperature ranges of 468.13-525 K, 392. 88-468.13 K, and 300-392.85 K, respectively. Next, the heights of each layer and crosssectional area ratio between the n-type and p-type TE legs should be optimized to obtain the same temperature differences in both the p-type and n-type TE legs and a uniform current density distribution. This is necessary to improve the overall performance of the module to compensate for the different TE properties of the p-type and n-type TE materials [72-74]. To find the optimal height of each layer that satisfies the given temperature distribution, a 3D FEA was conducted using COMSOL Multiphysics considering a 3D heat conduction model. The dimensions of the electrodes included in the model are 10 x 20 x 0.5 mm³, and the area of the three-layered TE leg is 5 x 5 mm² with a total height fixed at 5 mm. For the n-type TE leg, simulations were performed by sweeping the height of the bottom layer from 1.7 to 1.9 mm and the height of the middle layer from 1.2 to 1.4 mm, in increments of 0.01 mm. For the p-type TE leg, simulations were conducted by sweeping the height of the bottom layer from 1.7 to 1.9 mm and the height of the middle layer from 1.7 to 1.9 mm, also in increments of 0.01 mm. The temperature-dependent material properties of each composition in a TE leg measured in this work were interpolated using piecewise cubic to simulate. The electrical contact resistance between the TE leg and electrodes was applied using experimentally measured values. As boundary conditions, the hot-side temperature was maintained at 525 K and the cold-side temperature was maintained at 300 K. Similar to the vacuum condition, the lateral sides were subjected to adiabatic conditions. By varying the heights of the bottom and middle layers of the ntype and p-type TE legs, over 400 different combinations of the temperature distributions at the junctions for all these cases are shown in Fig. S7. We found that the smallest discrepancy of 0.025 % and 0.034 % between the target temperatures and the calculated temperatures of designed structures were obtained at the heights of n-type layers of 1.83 mm (Na0.175), 1.28 mm (Na0.1), and 1.89 mm (Na0). Similarly, for the p-type material, the optimum heights of each layer were identified to be 1.82 mm (Bi0.55), 1.76 mm (Bi0.5), and 1.42 mm (Bi0.35).

To optimize the cross-sectional areal ratio of the FGTEM module, the equation $ZT=S^2\sigma T/\kappa$ was reproduced using the areal term; $R=L_p/(\sigma_p A_p)+L_n/(\sigma_n A_n)$, $K=(\kappa_p A_p)/L_p+(\kappa_n A_n)/L_n$ where R and K are the electrical resistance and thermal conductance of the FGTEM module, respectively. When differentiated from A_n/A_p , ZT reaches its maximum value when the following equation is satisfied:

$$\frac{A_n}{A_p} = \left(\int_{T_c}^{T_h} \sqrt{\frac{\sigma_p(T)\kappa_p(T)}{\sigma_n(T)\kappa_n(T)}} \right) / (T_h - T_c)$$
 (1)

To validate the design derived from analytical calculations, we conducted the computation of the output power of the p-type and n-type TE legs at different A_p/A_n using the FEA models (Fig. S9). The results confirmed that the TE module is expected to achieve maximum power at an A_p/A_n ratio of approximately 0.96, which agrees with the calculated value from the Eq. (1).

3. Results and discussion

3.1. 3D printing of FGTEM

Dopant- and void-graded $Bi_2Te_{2.7}Se_{0.3}$ FGTEMs were fabricated via extrusion-based sequential 3D printing of all-inorganic inks in a layer-by-layer manner (Fig. 1a). The doping gradient was achieved by sequentially printing colloidal inks of $Bi_2Te_{2.7}Se_{0.3}$ particles with various Na concentrations. A printed single layer had a minimum thickness of 150 μ m, and a sequence of compositions containing $Bi_2Te_{2.7}Se_{0.3}$ doped with x wt% Na (x = 0, 0.05, 0.1, 0.15, 0.2, 0.25) was layered from top to bottom (Fig. 1b) to obtain the final FGTEM with dimensions of 2 mm \times 2 mm \times 1.5 mm. After high-temperature

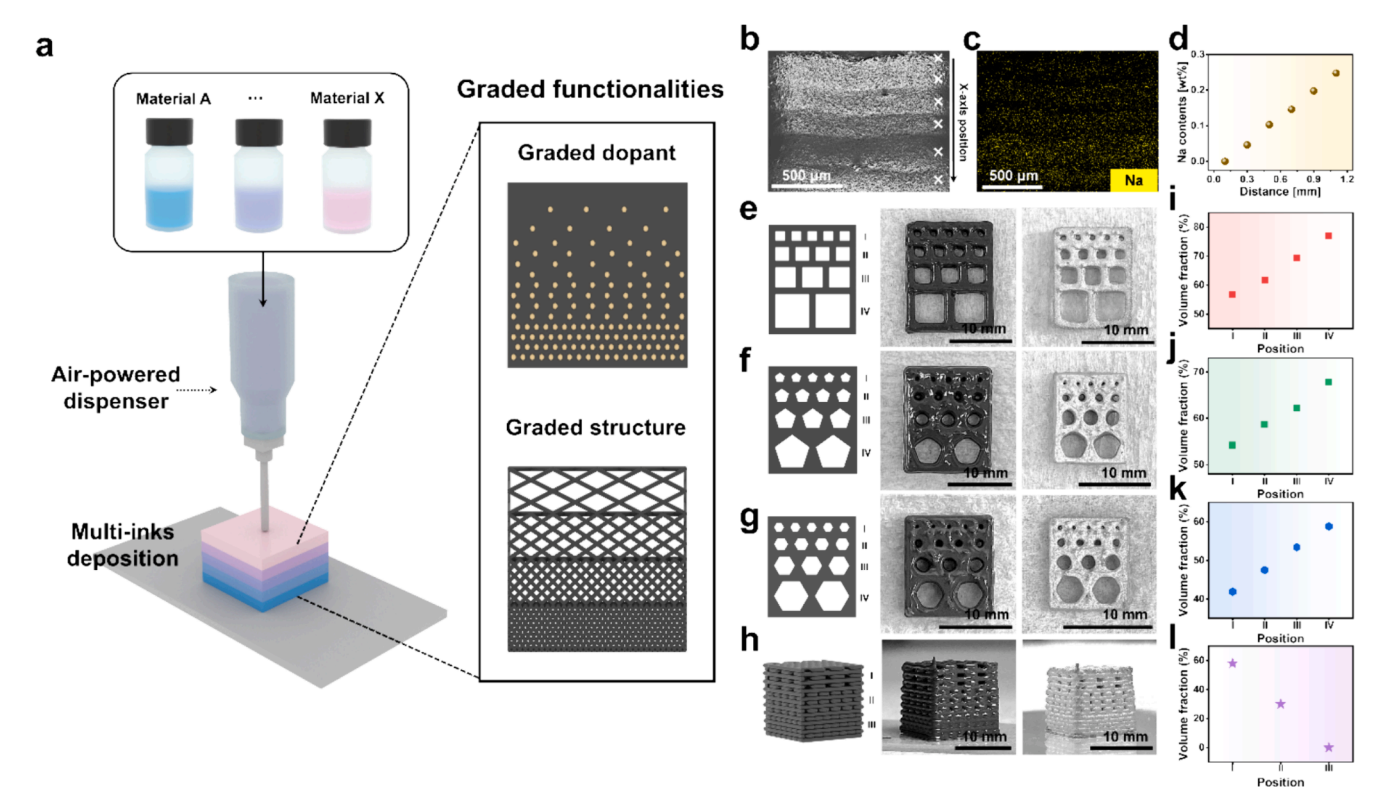


Fig. 1. Schematic of the extrusion-based 3D printing process for fabricating the electronic dopant-graded and structural void-graded FGTEM. (a) Sequential ink deposition with graded functionalities. (b) SEM image and (c) EDS mapping of 3D-printed Bi₂Te_{2.7}Se_{0.3} with layers containing six doping concentrations in the range 0–0.2 wt%. (d) Na doping concentration measured via EDS analysis of the six points indicated in (b). Structural void-graded FGTEM with voids of various shapes: (e) square, (f) pentagon, (g) hexagon in the horizontal direction and (h) void-gradient in the vertical direction. (i–l) Volume fractions of the voids according to positions I–IV of each FGTEM.

sintering at 783 K, the final sample had dimensions of 1.4 mm \times 1.4 mm \times 1.0 mm because of sintering shrinkage. Owing to the high reproducibility of the sintering shrinkage rate, the computer-aided design (CAD) model could be scaled before printing to ensure production of the desired FGM. The doping gradient in the printed sample was evaluated via EDS analysis (Fig. 1c), which showed that all printed layers exhibited Na doping concentrations identical to those of the printed TE inks. Accordingly, a linearly graded concentration of Na doping was achieved over the entire volume of the sample in the vertical direction (Fig. 1d). This dopant gradient enabled us to control the carrier concentration and, in turn, adjust the operable temperature ranges of the TE materials by suppressing or promoting the bipolar effect.

In addition to gradient engineering at the atomic scale, we demonstrated a macroscopic structural gradient in the printed FGTEM. Employing the CAD model, we generated a gradient consisting of a variety of macroscopic voids with sizes ranging from several hundreds of micrometers to several millimeters in the printed materials in both two and three dimensions, as shown in the photographs in Fig. 1e-h. In addition, we controlled the shapes of the voids (squares, pentagons, and hexagons) inside the printed material. On the basis of the size and shape of the voids, we could control the void formation such that fractions ranging from 0 % to 78 % were occupied by voids in the 2D-printed samples (Fig. 1i-k). Moreover, in the 3D-printed graded sample (Fig. 1h), the void gradient in the vertical direction was obtained by controlling the line spacing between the printed filaments in a lattice pattern, which enabled the void gradient to be varied from 0 % to 60 % (Fig. 11). These structural gradients could potentially affect electrical and thermal conductance, which would provide an additional engineering parameter for the optimization of the TE properties of the materials and devices.

The high structural integrity and precision of the 3D-printed

structures of the FGTEMs are attributed to their excellent 3D printability characteristics, such as the diameter of the printed filament, line-to-line resolution, and homogeneous sintering shrinkage. The diameter of the printed filament was varied from 200 µm to more than 1 mm by controlling the nozzle diameter or extrusion pressure (Fig. 2a and 2d, Fig. S1), whereby an almost linear relationship could be established between the diameter of the nozzle and that of the printed filament (Fig. 2d). The filament diameter decreased uniformly after sintering at 783 K for 3 h (Fig. 2b). This sintering shrinkage enabled strong bonding between the printed layers, a crucial factor for implementing structural or dopant gradients in the horizontal or vertical direction without the need for a separate complex joining process. Regardless of the filament diameter, the filaments exhibited almost identical sintering shrinkage of 29.5 %, in good agreement with the volumetric shrinkage observed in the bulk sample (Fig. 1b). In addition, controlling the diameter of the printed filaments in a 3D lattice presented a simple way to control the volume of the void among the filaments. As seen in the OM images (Fig. 2c), the projected areas of the voids between the printed lattices progressively narrowed as the diameter of the printed filament increased (Fig. 2f). These results demonstrate the feasibility of using our 3D printing process to manufacture FGMs efficiently in a cost-effective manner.

3.2. Formulation and characterizations of TE inks

The TE inks for 3D printing were formulated by preparing a colloidal dispersion of the synthesized Na-doped $\rm Bi_2Te_{2.7}Se_{0.3}$ microparticles, which were synthesized by alloying elemental Bi, Te, and Se (that contained the desired Na doping concentrations of 0, 0.1, 0.15, 0.175, and 0.2 wt%) in a mechanical process. The XRD patterns of the synthesized particles, shown in Fig. S2a, correspond well with those of bulk

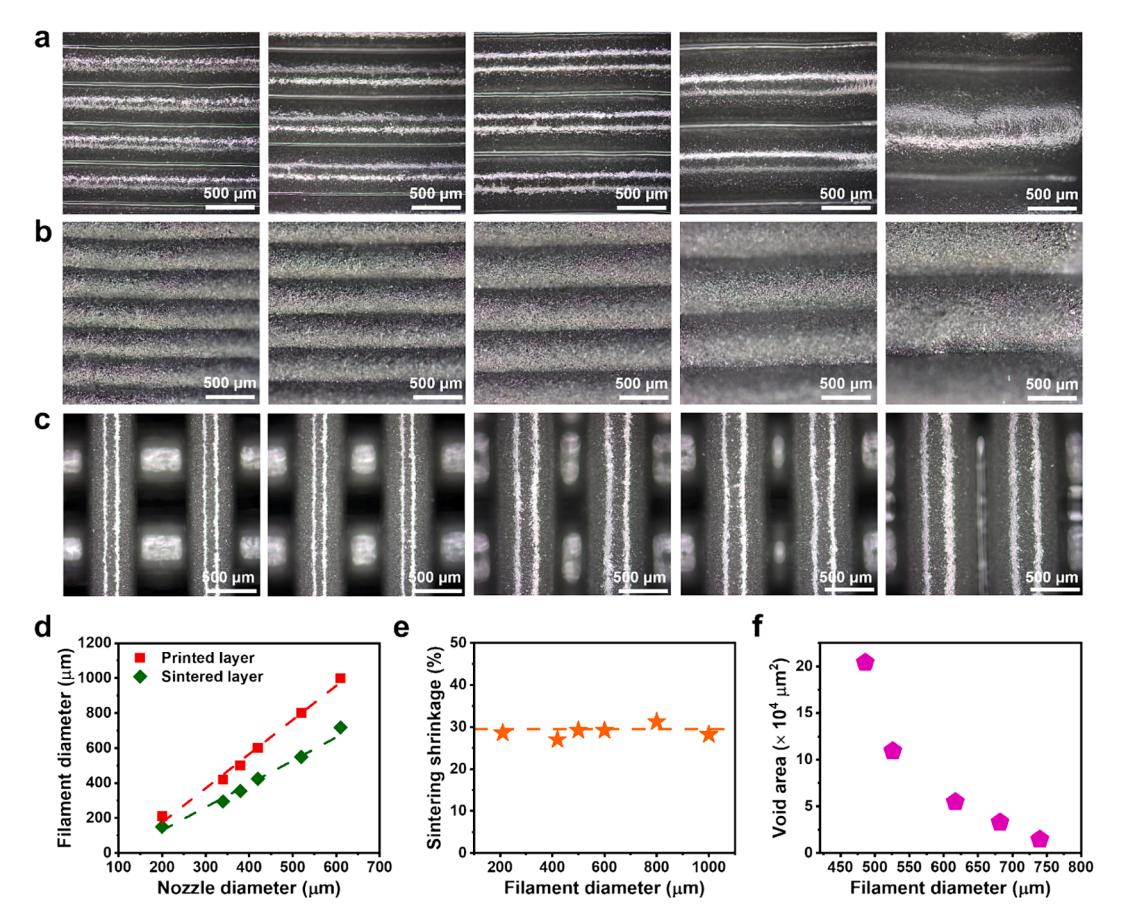


Fig. 2. Controllability of 3D printing parameters for fabricating the FGTEM. OM images of the (a) 3D-printed, (b) sintered filaments for various nozzle diameters, and (c) filaments printed in a lattice pattern according to different extrusion pressures. (d) Diameters of 3D-printed and sintered TE filaments depending on the nozzle diameter. The dashed lines are linear fittings of each point in the printed and sintered layer. (e) Sintering shrinkage versus filament diameter, calculated using the following equation: sintering shrinkage = $(1 - \text{sintered filaments diameter/printed filaments diameter}) \times 100$ (%), and the dashed line was calculated with the fitted graph in (d). (f) Projected void area vs. diameter of the printed filaments.

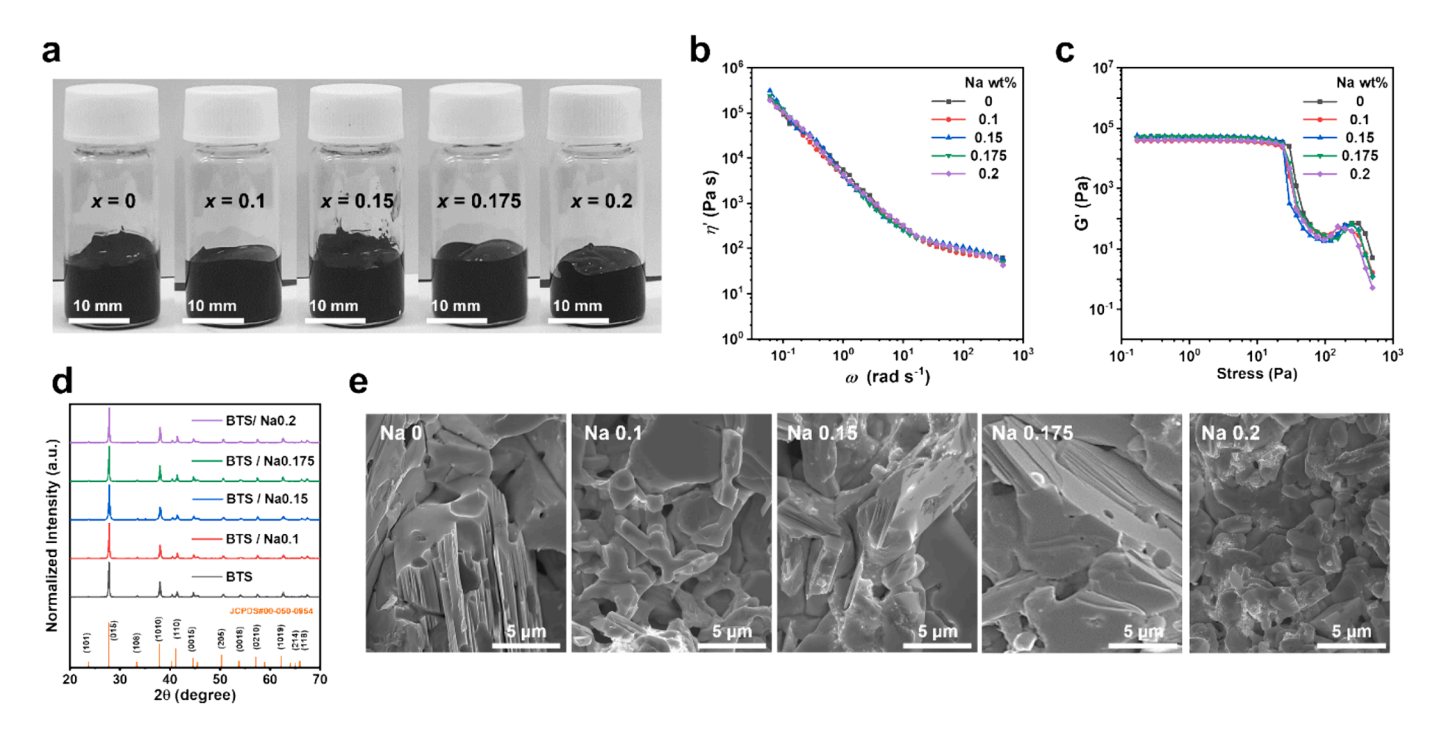


Fig. 3. Characterization of inks and materials with various Na doping concentrations. (a) Photographic images, (b) dynamic viscosity, and (c) storage modulus of TE inks. (d) XRD patterns and (e) SEM images of the microstructures of the 3D-printed samples.

Bi₂Te_{2.7}Se_{0.3} without any additional peaks related to impurities. Of particular interest is that the XRD peaks shifted according to the Na concentration. As evident from the enlarged XRD pattern, the (015) peak of the undoped alloy at $\sim 28^{\circ}$ initially shifted to a lower angle for a Na concentration of 0.1 wt%, followed by progressive shifts to higher angles with increasing Na concentration (Fig. S2b). This structural behavior corresponds well with previous observations of Na-doped Bi₂Te₃ bulk materials [61]. Moreover, an increase in the Na concentration is reportedly accompanied by a decrease in the formation energy of Te vacancies. This is ascribed to the increasing difference in the electronegativity between the anions and cations, which ultimately increases the concentration of Te vacancy defects [75]. This dopinginduced formation of defects was responsible for the progressive shift of the peaks to higher angles in the XRD patterns caused by lattice shrinkage. In contrast, at a Na concentration of 0.1 wt%, the Bi_{Te} antisite defects, which form when Bi with its larger atomic radius occupies vacant Te sites, predominated over Te vacancies. This increased the distance between the layers inside the crystal and thus the lattice constant. This competitive formation of Te vacancies and Bi_{Te} antisites, depending on the Na concentration, is considered responsible for the peak shifts in the XRD patterns.

Rheological viscoelasticity is a crucial requirement for the application of inks in the 3D printing of architectures via layer-by-layer deposition (Fig. 3a). We improved the viscosity of the ink by exploiting the electroviscous effect by introducing chalcogenidometallate (ChaM) Sb₂Te₄²⁻ complexes as inorganic additives to provide surface charges to the particles [76]. The rheology of the ink doped with Na was measured using a rheometer, and these results are depicted in Fig. 3b,c. The rheology was assessed by determining the dynamic viscosity and storage modulus. The former denotes the absolute magnitude of the resistance of the fluid to flow in the direction of motion, whereas the latter quantifies the extent to which a material responds elastically to external deformation. The measurements revealed that, regardless of the Na doping

concentration, the rheological properties of the ink were similar, with a dynamic viscosity of $2\text{--}3 \times 10^5$ Pa s and a storage modulus of $4.2\text{--}5.8 \times 10^4$ Pa. The rheology of the ink is closely related to the surface charge of its particles, which suggests that doping with Na does not significantly affect the surface charge of the TE inks. After 3D printing using the viscoelastic TE inks, the printed samples were sintered in a box furnace at 783 K for 3 h. The sintered samples with different Na concentrations also exhibited no second-phase peaks in their XRD patterns (Fig. 3d). SEM images (Fig. 3e and Fig. S3) revealed that all the samples were well sintered and had grains with sizes ranging from several to several tens of micrometers. The effectiveness of the sintering was further supported by the fact that the samples had a relative density of 70 %–75 % (Fig. S4), which is significantly higher than the values reported for 3D-printed n-type Bi₂Te₃ [76–78].

We further measured the mechanical properties of $0.1~\rm wt\%$ Na doped and undoped samples by a compressive strength test. As shown in Fig. S5, both samples exhibited almost similar behaviors in the strain–stress curves, resulting in similar Young's modulus and compressive strength. This result demonstrates that the Na doping doesn't affect the mechanical properties of the samples.

3.3. TE properties of Bi₂Te_{2.7}Se_{0.3} doped with different amounts of Na

To verify that the carrier concentration could be controlled via Na doping, room-temperature Hall effect measurements were conducted on 3D-printed Bi $_2$ Te $_2.7$ Se $_0.3$ with Na doping concentrations of 0–0.2 wt%. An increase in the Na concentration from 0 to 0.2 wt% caused the electron concentration of the 3D-printed samples to gradually decrease from 5.5 \times 10 19 cm $^{-3}$ to 2.2 \times 10 19 cm $^{-3}$. This clearly indicates the electron dedoping effect of the Na impurity (Fig. 4a). Na doping of Bi $_2$ Te $_3$ -based materials lowers the formation energy of Na $_{\rm Te}$ or Bi $_{\rm Te}$ antisites. These anti-sites act as hole dopants to increase the concentration of minority hole carriers and decrease the electron

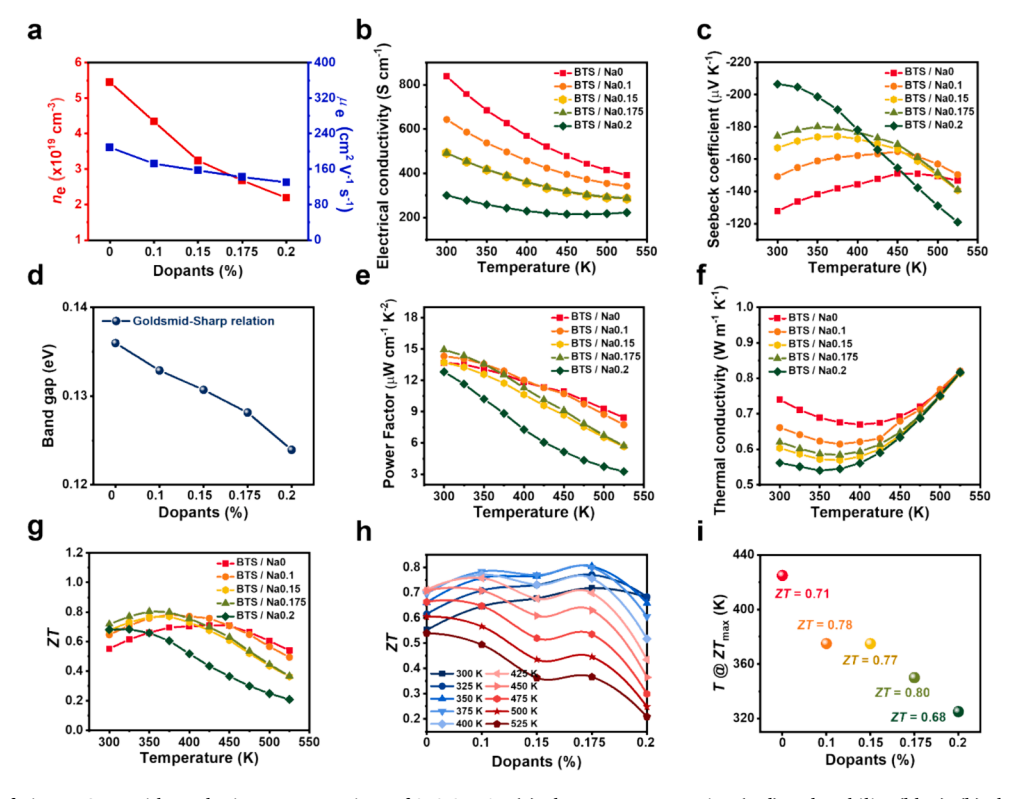


Fig. 4. TE properties of $Bi_2Te_{2.7}Se_{0.3}$ with Na doping concentrations of 0–0.2 wt%. (a) Electron concentration (red) and mobility (blue), (b) electrical conductivity vs. temperature, (c) Seebeck coefficient vs. temperature, (d) estimated band gap by Goldsmid-Sharp relation, (e) power factor vs. temperature, (f) thermal conductivity vs. temperature, (g) figure of merit, ZT for various Na doping concentrations. (h) ZT profiles vs. Na concentration at selected temperatures in the range 300–525 K, and (i) temperature at which the TE materials have a maximum ZT value and dependence on the Na doping concentration.

concentration. This behavior corresponds with previous results for Nadoped $\rm Bi_2Te_3$ bulk materials synthesized via the melting method [61]. Additionally, the electron mobility of the 3D-printed samples doped with 0–0.2 wt% Na decreased from 209 cm² V $^{-1}$ s $^{-1}$ to 130 cm² V $^{-1}$ s $^{-1}$. This reduction in the carrier mobility can be attributed to intensified impurity scattering by the Na dopant and formation of defects, such as anti-sites and vacancies.

The controllable changes in the electron concentration owing to Na doping are clearly reflected in the electrical properties of the 3D-printed samples. As expected, the room-temperature electrical conductivities of the samples gradually decreased as the Na doping concentration increased from 0 to 0.2 wt%. For example, the pristine undoped Bi₂Te_{2.7}Se_{0.3} sample had an electrical conductivity of 837 S cm⁻¹ at room temperature, whereas 300 S cm⁻¹ was measured for the Bi₂Te_{2.7}Se_{0.3} doped with 0.2 wt% Na. The dependence of the conductivity on the doping concentration is attributed to changes in the electron concentration and mobility because the electrical conductivity is defined by the equation $\sigma = en\mu$, where σ represents the electrical conductivity, e is electric charge, n is the electron concentration, and μ represents the electron mobility. Furthermore, the electrical conductivity of all the samples was inversely related to the temperature, a property that is commensurate with the characteristics of a degenerate semiconductor (Fig. 4b) and in agreement with that of previously reported Bi₂Te₃-based materials [60-71,76-81]. Additionally, the temperature dependence weakened for samples with a higher Na doping concentration. This is understandable, considering that the bipolar contribution to the electrical conductivity at higher temperatures intensifies as the electron concentration decreases. The electrical conductivities of 0.15 and 0.175 wt% Na doped Bi₂Te_{2.7}Se_{0.3} exhibit similarity, although they are not precisely identical (Table S1). Despite variations in electron concentrations and mobilities between these samples (Fig. 4a), their resulting electrical conductivities fortuitously align.

The Seebeck coefficients at room temperature increased with increasing Na concentration for all samples, as shown in Fig. 4c. In particular, the Seebeck coefficient of undoped Bi₂Te_{2.7}Se_{0.3} is approximately $-130\mu V K^{-1}$, whereas that of Bi₂Te_{2.7}Se_{0.3} doped with 0.2 wt% Na reached $-208\mu V K^{-1}$. This dependence on the doping concentration can be understood by considering that the Seebeck coefficient and electron concentration have reciprocal proportions. That is, the temperature at which the Seebeck coefficient is maximized decreased with increasing doping concentration because of the decreased electron concentration, which promoted the bipolar contribution. The undoped sample exhibits a maximum Seebeck coefficient at 450 K, whereas the sample doped with 0.2 wt% Na reaches its maximum at room temperature, indicating the occurrence of the bipolar effect at room temperature. This bipolar contribution can be quantitatively understood by considering that the band gap (E_g) varies depending on the doping concentration. This suggests that the bipolar effect should be more pronounced in a material with a narrower E_g owing to the intrinsic excitation at a given temperature. We used the Goldsmid-Sharp equation, $E_g = 2e|S_{\rm max}|T_{\rm max}$ [82], where $S_{\rm max}$ is the maximum value of the Seebeck coefficient at the temperature (T_{max}), to calculate the band gap of the Bi₂Te_{2.7}Se_{0.3} samples doped with Na. The calculations showed that the band gaps of the samples became progressively narrower with increasing doping concentration and could be responsible for the changes in the electrical properties, most likely due to the bipolar contribution. The similarity of the maximum power factors (σS^2) of the samples, which ranged from 13 to 15µW cm⁻¹ K⁻², was considered to compensate for the electrical properties of each sample. For example, the sample doped with 0.175 wt% Na at room temperature had the highest power factor owing to its relatively large Seebeck coefficient, although its electrical conductivity was lower than that of the undoped sample (Fig. 4e).

To further understand the Na doping effect on the Seebeck coefficient, the effective masses (m^*) of the samples were calculated using the

following equation,

$$S = \frac{8\pi^2 k_B^2}{3eh^2} m^* T \left(\frac{\pi}{3n}\right)^{\frac{2}{3}} \tag{2}$$

where S, k_B , T, m^* , e, h and n are the Seebeck coefficient, Boltzmann's constant, absolute temperature, effective mass, electronic charge, Planck's constant and electron concentration [83]. The Seebeck coefficient is generally determined by the effective mass of carriers as well as their concentrations. The calculated effective masses for all samples are almost identical, and the only slight variation was observed (Table S2). Moreover, the carrier concentration dependence of the Seebeck coefficient is illustrated by the Pisarenko plot at 300 K (Fig. S6). The solid curve was generated with an effective mass of $m^* = 0.85 \ m_0$, that was the calculated values for the properties of the 0.1 wt% Na doped Bi $_2$ Te $_2$,7Se $_0$,3 samples. The Seebeck coefficients of all samples at room temperature are merged in the solid curve, suggesting that the variation of carrier concentrations played a main role to change the Seebeck coefficient.

The thermal conductivities of the Na-doped samples depended similarly on the electrical conductivity, with the values increasing with decreasing Na doping concentration. At low temperatures, with increasing the Na doping content, the thermal conductivity of the samples decreased. This doping-dependent thermal conductivity could be attributed to the Na impurity scattering of phonons, reducing the thermal conductivity. On the other hand, at high temperature range (400-525 K), a bipolar effect was observed for the temperature dependence of the thermal conductivity, which increased faster with temperature for a sample with a higher doping concentration. Since the intrinsic thermal excitation of minority carriers are promoted at high temperature, the larger number of holes in our samples could contribute to the heat transport as a bipolar thermal conductivity. As a consequence, the thermal conductivity of all samples became similar at the highest measurement temperature of 525 K. The lowest thermal conductivity of 0.54 W m⁻¹ K⁻¹ was measured for the sample with a Na doping concentration of 0.2 wt%, which is significantly lower than that of the undoped Bi₂Te_{2.7}Se_{0.3} (Fig. 4f).

Consequently, the calculated temperature-dependent ZT values clearly varied in the operable temperature ranges depending on the doping concentration. For example, the temperature at which the ZT value was maximized increased from 300-325 K for the sample doped with 0.2 wt% Na to 425-450 K for the undoped sample. Among all the samples, the sample doped with 0.175 wt% Na had the highest ZT value of 0.8 at 350 K (Fig. 4g), which is comparable with that of bulk Bi₂Te_{2.7}Se_{0.3} synthesized via traditional bulk processes such as hotpressing and zone-melting [84-87]. Moreover, this maximum was significantly enhanced by Na doping compared with the 0.71 of the undoped sample. We additionally plotted the calculated ZT values vs. the Na concentration at selected temperatures (Fig. 4h), which served to determine the optimal dopant level in a particular temperature range. On this graph, the room-temperature ZT values gradually increase with increasing Na doping concentration, whereas the ZT values at 525 K show the opposite trend, thereby indicating the effect of doping on the ZT values. The temperature at which the ZT value is maximized for each doping concentration was plotted (Fig. 4i) and shows the tunability of the operable temperature range by adjusting the amount of dopant. This tunability enabled us to optimize the structures in the FGTEM such that the power-generating performance was maximized over a wide temperature range.

3.4. Fabrication and power measurement of FGTEM module

Our sequential 3D printing technology facilitates the manufacturing of FGTEMs with high-precision gradient profiles in a rapid, direct, and cost-effective manner (Supplementary video 1). Moreover, the tunability of the property gradient of the material enables the design of

TE legs with high efficiency to maximize the average ZT and resulting output power of the FGM. Based on the temperature dependence of the TE properties of our samples, we designed the optimum FGM leg by considering two design parameters: i) doping engineering to fine-tune the peak ZTs for a wider range of temperatures and ii) geometrical engineering to optimize the dimensions of the TE legs for a uniform current density distribution and to improve the overall performance of the module (Fig. 5b-c and Fig. S8, S9). We attempted to fabricate a TEG consisting of multiple n-type Bi₂Te_{2.7}Se_{0.3} legs with a dopant gradient in combination with a p-type $Bi_vSb_{2-v}Te_3$ leg with a composition gradient. The respective components of the p- and n-type FGTEM exhibited similar compatibility factors (Fig. S10), thereby indicating that they are suitable for the fabrication of graded TE modules [47]. We succeeded in fabricating a $Bi_2Te_{2.7}Se_{0.3}$ leg with a doping gradient with three Na concentrations. This composition extended the temperature range of the peak ZTs to achieve an average ZT value of 0.71 over a broad temperature range from 300 K to 525 K, which was an improvement of approximately 10 % compared with the ZT value of a homogeneous TE material (Fig. 5d).

A TEG chipped with legs comprising an n-type FGTEM with a doping gradient and p-type FGTEM with a composition gradient, precisely 3D printed according to the design specifications, was fabricated with Cu electrodes using Sn/Ag/Cu solder (Fig. 5a). Although the contact resistance between the TE leg and electrode was negligible, we considered this when determining the geometric design of the TEG. The performance of the TEG was assessed under controlled conditions, where the top electrode was heated using a ceramic heater and the bottom electrodes were cooled using a water-circulating cooler. The hot-side temperature was increased gradually from 297.65 K to 523.27 K while the cold-side temperature was maintained at 298.15 K with a variation of less than \pm 1 K. Fig. S11 shows the hot- and cold-side temperature profiles. The system was monitored until it reached the steady state, at which point the temperature fluctuation was < 0.5 K. The module resistance was measured to be 6.3 m Ω at room temperature, which was

almost the same as the value predicted by the simulation. In addition, the module resistance versus the temperature difference (ΔT) was also similar to the simulation data (Fig. S12a). For instance, for a ΔT of 224.96 K (Fig. 5e), the maximum voltage and output power measured for the FGTEM module were 86.1 mV and 187 mW, respectively. Compared with the properties of the homogeneous material TEG consisting of p-type Bi_{0.35}Sb_{1.65}Te₃ and n-type Bi₂Te_{2.7}Se_{0.3} doped with 0.175 wt% Na, those of the FGTEM module at a ΔT of 224.96 K were superior, with a maximum power density of 357 mW cm⁻², which is 20 % higher than that of the homogeneous TEG (Fig. S13). These values are highly consistent with the simulated values (Fig. S13). The slight deviation from the experimental results could be attributed to the measurement uncertainty of the temperatures and the assumption for the simulation, where the perfect adiabatic condition was assumed.

4. Conclusion

We developed a sequential 3D printing method to fabricate the graded n-type Bi₂Te_{2.7}Se_{0.3} TE materials with electronic dopant and structural void gradients. The synthesized Bi₂Te_{2.7}Se_{0.3} TE particles, with controlled Na-doping concentrations, were used for the formulation of inks. These inks, which were highly viscoelastic and suitable for 3D printing regardless of the Na-doping concentration, enabled the use of filaments with a minimum diameter of 150 µm for printing 3D structures. Using sequential 3D printing, we fabricated an FGTEM with a gradient of atomic Na doping concentrations or structural voids in a layer-by-layer manner. Furthermore, the ZT peak temperatures of the 3D-printed TE materials varied controllably depending on the Na concentration and high average ZT values were achieved over a wide temperature range by introducing a doping gradient in the 3D-printed materials. Combined with the p-type BiSbTe material with a composition gradient, the fabricated power generator chipped with the 3Dprinted n-type Bi₂Te_{2.7}Se_{0.3} material with the optimal doping gradient had substantially higher output power compared with those of the

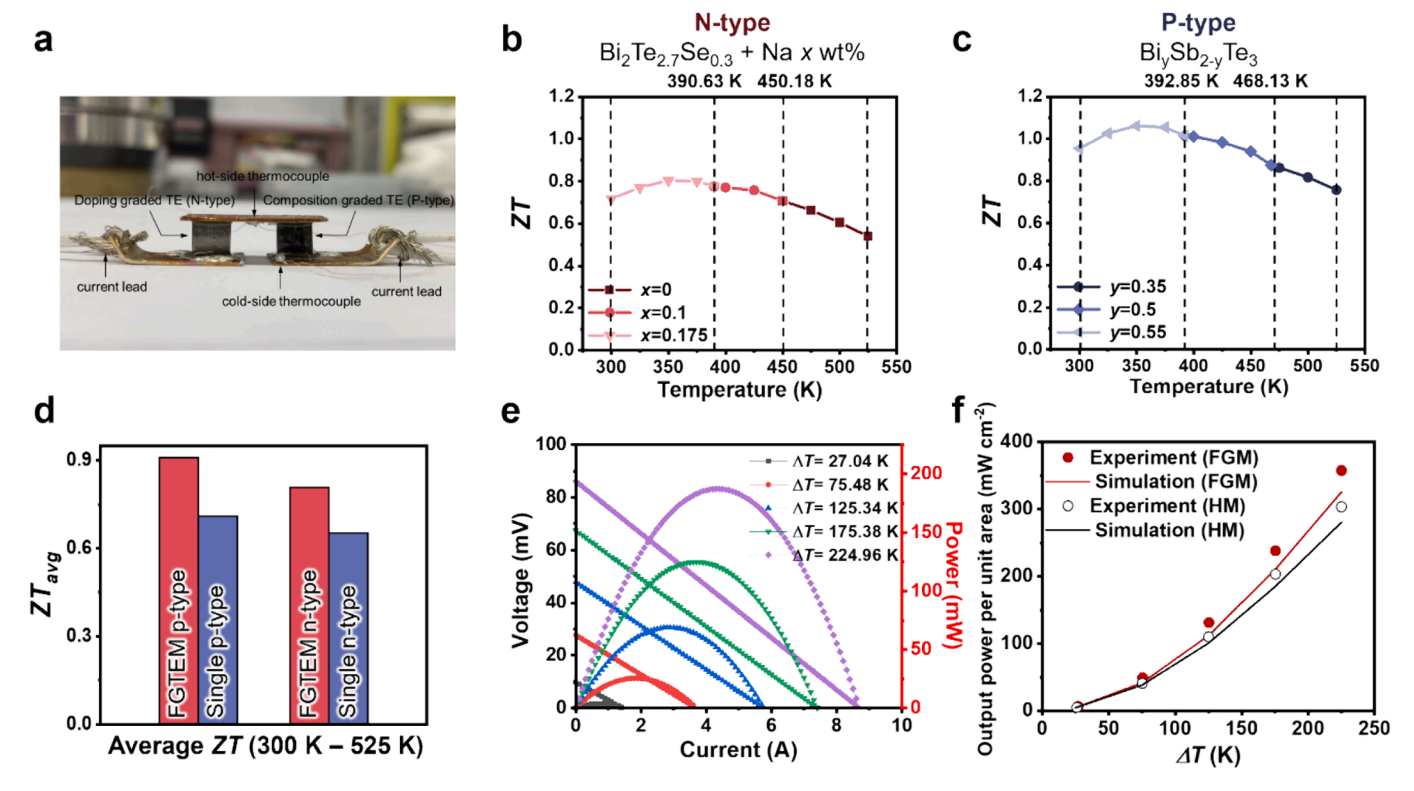


Fig. 5. Power performance measurement of FGTEM module. (a) Photograph of FGTEM module and (b–c) compiled ZT values for three compositions of n- and p-type FGTEMs, respectively. (d) Comparison of the average ZT value of p- and n-type FGTEMs with that of the homogeneous material. (e) Output voltage and power of FGTEM module for various ΔT , and (f) output power density of FGTEM module and homogeneous material TEG compared with simulation data.

device chipped with ungraded homogeneous materials. Our 3D sequential printing method offers a rapid and cost-effective way to manufacture FGTEMs with customized shapes and precisely controlled composition, doping, and structure gradients, which can extend the application of FGTEMs to energy and electronic devices beyond that of structural materials.

CRediT authorship contribution statement

Hyunjin Han: Writing – original draft, Methodology, Investigation, Formal analysis, Data curation, Conceptualization. Seong Eun Yang: Writing – original draft, Validation, Methodology, Investigation, Data curation, Conceptualization. Jungsoo Lee: Software, Methodology. Keonkuk Kim: Methodology. Changhyeon Nam: Methodology. Seungki Jo: Methodology. So-Hyeon Lee: Methodology. Ju-Young Kim: Methodology. Sangjoon Ahn: Methodology. Jae Sung Son: Writing – review & editing, Writing – original draft, Validation, Supervision, Funding acquisition, Conceptualization.

Declaration of competing interest

The authors declare that they have no known competing financial interests or personal relationships that could have appeared to influence the work reported in this paper.

Data availability

Data will be made available on request.

Acknowledgements

This work was supported by the National Research Foundation of Korea (NRF), South Korea funded by the Ministry of Science and ICT of Republic of Korea (NRF-2021M3C1C3097541; NRF-2022M3C1A3091988) and the Korea Research Institute of Chemical Technology (No. SS2222-20).

Appendix A. Supplementary data

Supplementary data to this article can be found online at https://doi.org/10.1016/j.cej.2024.154547.

References

- [1] N.W. Bartlett, M.T. Tolley, J.T.B. Overvelde, J.C. Weaver, B. Mosadegh, K. Bertoldi, G.M. Whitesides, R.J. Wood, A 3D-printed functionally graded soft robot powered by combustion, Science. 349 (6244) (2015) 161–165, https://doi.org/10.1126/ science.aab0129
- [2] P.A.G.S. Giachini, S.S. Gupta, W. Wang, D. Wood, M. Yunusa, E. Baharlou, M. Sitti, A. Menges, Additive manufacturing of cellulose-based materials with continuous, multidirectional stiffness gradients, Sci. Adv. 6(8) (2020) eaay0929, http://doi. org/10.1126/sciadv.aay0929.
- [3] Y. Li, Z. Feng, L. Hao, L. Huang, C. Xin, Y. Wang, E. Bilotti, K. Essa, H. Zhang, Z. Li, F. Yan, T. Peijs, A review on functionally graded materials and structures via additive manufacturing: from multi-scale design to versatile functional properties, Adv. Mater. Technol. 5 (2020) 1900981, https://doi.org/10.1002/admt.201900981.
- [4] J.C. Agar, A.R. Damodaran, M.B. Okatan, J. Kacher, C. Gammer, R.K. Vasudevan, S. Pandya, L.R. Dedon, R.V.K. Mangalam, G.A. Velarde, S. Jesse, N. Balke, A. M. Minor, S.V. Kalinin, L.W. Martin, Highly mobile ferroelastic domain walls in compositionally graded ferroelectric thin films, Nat. Mater. 15 (2016) 549–556, https://doi.org/10.1038/mmat4567.
- [5] A.R. Damodaran, S. Pandya, Y. Qi, S.-L. Hsu, S. Liu, C. Nelson, A. Dasgupta, P. Ercius, C. Ophus, L.R. Dedon, J.C. Argar, H. Lu, J. Zhang, A.M. Minor, A. M. Rappe, L.W. Martin, Large polarization gradients and temperature-stable responses in compositionally-graded ferroelectrics, Nat. Commun. 8 (1) (2017) 14961, https://doi.org/10.1038/ncomms14961.
- [6] Z. Tong, Y. Xie, M.C. Arno, Y. Zhang, I. Manners, R.K. O'Reilly, A.P. Dove, Uniform segmented platelet micelles with compositionally distinct and selectively degradable cores, Nat. Chem. 15 (6) (2023) 824–831, https://doi.org/10.1038/ s41557-023-01177-2.

- [7] L. Xing, Y. Xu, Ž. Penga, Q. Xu, H. Su, F. Barbir, W. Shi, J. Xuan, A segmented fuel cell unit with functionally graded distributions of platinum loading and operating temperature, Chem. Eng. J. 406 (2021) 126889, https://doi.org/10.1016/j. cei 2020 126889
- [8] M. Patel, P. Bharti, P. Prabhakar, S. Shrivastava, P. Mehar, P. Kumar, D. Mondal, A. K. Srivastava, C. Dhand, N. Dwivedi, Functionally gradient multilayer coating enabled flexible sensors for lead detection in water and soil, Chem. Eng. J. 483 (2024) 149441, https://doi.org/10.1016/j.cej.2024.149441.
- [9] J. Liu, J. Zhou, M. Wang, C. Niu, T. Qian, C. Yan, A functional-gradient-structured ultrahigh modulus solid polymer electrolyte for all-solid-state lithium metal batteries, J. Mater. Chem. a. 7 (42) (2019) 24477–24485, https://doi.org/ 10.1039/c9ta078776b
- [10] A. Kamtsikakis, J. Baales, V.V. Zeisler-Diehl, D. Vanhecke, J.O. Zoppe, L. Schreiber, C. Weder, Asymmetric water transport in dense leaf cuticles and cuticle-inspired compositionally graded membranes, Nat. Commun. 12 (1) (2021) 1267, https:// doi.org/10.1038/s41467-021-21500-0.
- [11] M. He, Q. Wang, L. Xie, H. Wu, W. Zhao, W. Tian, Hierarchically multifunctionalized graded membrane with enhanced bone regeneration and selfdefensive antibacterial characteristics for guided bone regeneration, Chem. Eng. J. 398 (2020) 125542, https://doi.org/10.1016/j.cej.2020.125542.
- [12] J. Du, X. Niu, N. Rahbar, W. Soboyejo, Bio-inspired dental multilayers: Effects of layer architecture on the contact-induced deformation, Acta Biomater. 9 (2) (2013) 5273–5279, https://doi.org/10.1016/j.actbio.2012.08.034.
- [13] M. Trofa, E. Di Maio, P.L. Maffettone, Multi-graded foams upon time-dependent exposition to blowing agent, Chem. Eng. J. 362 (2019) 812–817, https://doi.org/ 10.1016/j.cej.2019.01.077.
- [14] M. Koizumi, FGM activities in Japan, Compos. b. Eng. 28 (1–2) (1997) 1–4, https://doi.org/10.1016/S1359-8368(96)00016-9.
- [15] P.H. Cong, T.M. Chien, N.D. Khoa, N.D. Duc, Nonlinear thermomechanical buckling and post-buckling response of porous FGM plates using Reddy's HSDT, Aerosp. Sci. Technol. 77 (2018) 419–428, https://doi.org/10.1016/j. ast.2018.03.020.
- [16] S. Kumar, K.M. Reddy, A. Kumar, G.R. Devi, Development and characterization of polymer–ceramic continuous fiber reinforced functionally graded composites for aerospace application, Aerosp. Sci. Technol. 26 (1) (2013) 185–191, https://doi. org/10.1016/j.ast.2012.04.002.
- [17] P. Srinivas, P.R. Babu, B. Balakrishna, Effect of silicon carbide, magnesium oxide as reinforcing elements and zinc sterate as binding agent in the characterization of Al functionally graded materials for automotive applications, Mater. Today. Proc. 27 (2020) 460–466. https://doi.org/10.1016/j.matpr.2019.11.275.
- [18] A. Arsha, E. Jayakumar, T. Rajan, V. Antony, B. Pai, Design and fabrication of functionally graded in-situ aluminium composites for automotive pistons, Mater. Des. 88 (2015) 1201–1209, https://doi.org/10.1016/j.matdes.2015.09.099.
- [19] E.S. Chin, Army focused research team on functionally graded armor composites, Mater. Sci. Eng. a. 259 (2) (1999) 155–161, https://doi.org/10.1016/S0921-5093 (98)00883-1.
- [20] S. Chandrasekaran, S. Hari, M. Amirthalingam, Wire arc additive manufacturing of functionally graded material for marine risers, Mater. Sci. Eng. a. 792 (2020) 139530, https://doi.org/10.1016/j.msea.2020.13953.
- [21] M. Abdi-Jalebi, M. Ibrahim Dar, S.P. Senanayak, A. Sadhanala, Z. Andaji-Garmaroudi, L.M. Pazos-Outón, J.M. Richter, A.J. Pearson, H. Sirringhaus, M. Grätzel, R.H. Friend, Charge extraction via graded doping of hole transport layers gives highly luminescent and stable metal halide perovskite devices, Sci. Adv. 5(2) (2019) eaav2012, https://doi.org/10.1126/sciadv.aav2012.
- [22] R. Konno, S. Maruyama, T. Kosaka, R. Katoh, R. Takahashi, H. Kumigashira, N. Ichikuni, H. Onishi, Y. Matsumoto, Artificially designed compositionally graded Sr-doped NaTaO₃ single-crystalline thin films and the dynamics of their photoexcited electron-hole pairs, Chem. Mater. 33 (1) (2020) 226–233, https:// doi.org/10.1021/acs.chemmater.0c03487.
- [23] X. Qi, J. Chen, K. Guo, S. He, J. Yang, Z. Li, J. Xing, J. Hu, H. Luo, W. Zhang, J. Luo, Thermal stability of Ag₉GaSe₆ and its potential as a functionally graded thermoelectric material, Chem. Eng. J. 374 (2019) 494–501, https://doi.org/ 10.1016/j.cej.2019.05.179.
- [24] E. Hazan, O. Ben-Yehuda, N. Madar, Y. Gelbstein, Functional graded germanium-lead chalcogenide-based thermoelectric module for renewable energy applications, Adv. Energy. Mater. 5 (11) (2015) 1500272, https://doi.org/ 10.1002/aenm.201500272.
- [25] E.M. Hedegaard, A.A. Mamakhel, H. Reardon, B. Iversen, Functionally graded (PbTe)_{1-x}(SnTe)_x thermoelectrics, Chem. Mater. 30 (1) (2018) 280–287, https://doi.org/10.1021/acs.chemmater.7b04473.
- [26] B. Cook, T. Chan, G. Dezsi, P. Thomas, C. Koch, J. Poon, T. Tritt, R. Venkatasubramanian, High-performance three-stage cascade thermoelectric devices with 20% efficiency, J. Electron. Mater. 44 (2015) 1936–1942, https://doi. org/10.1007/s11664-014-3600-9.
- [27] E.M. Hedegaard, S. Johnsen, L. Bjerg, K.A. Borup, B.B. Iversen, Functionally graded Ge_{1-x}Si_x thermoelectrics by simultaneous band gap and carrier density engineering, Chem. Mater. 26 (17) (2014) 4992–4997, https://doi.org/10.1021/ cm502042e
- [28] C.L. Cramer, H. Wang, K. Ma, Performance of functionally graded thermoelectric materials and devices: A review, J. Electron. Mater. 47 (2018) 5122–5132, https://doi.org/10.1007/s11664-018-6402-7.
- [29] M. Naebe, K. Shirvanimoghaddam, Functionally graded materials: A review of fabrication and properties, Appl. Mater. Today. 5 (2016) 223–245, https://doi.org/ 10.1016/j.apmt.2016.10.001.
- [30] B. Saleh, J. Jiang, R. Fathi, T. Al-hababi, Q. Xu, L. Wang, D. Song, A. Ma, 30 Years of functionally graded materials: An overview of manufacturing methods,

- Applications and Future Challenges, Compos. b. Eng. 201 (2020) 108376, https://doi.org/10.1016/j.compositesb.2020.108376.
- [31] X. Kuang, J. Wu, K. Chen, Z. Zhao, Z. Ding, F. Hu, D. Fang, H.J. Qi, Grayscale digital light processing 3D printing for highly functionally graded materials, Sci. Adv. 5(5) (2019) eaav5790, https://doi.org/10.1126/sciadv.aav5790.
- [32] Z. Wang, Z. Wang, Y. Zheng, Q. He, Y. Wang, S. Cai, Three-dimensional printing of functionally graded liquid crystal elastomer, Sci. Adv. 6(39) (2020) eabc0034, https://doi.org/10.1126/sciadv.abc0034.
- [33] C. Zhang, F. Chen, Z. Huang, M. Jia, G. Chen, Y. Ye, Y. Lin, W. Liu, B. Chen, Q. Shen, L. Zhang, E.J. Larvernia, Additive manufacturing of functionally graded materials: A review, Mater. Sci. Eng. a. 764 (2019) 138209, https://doi.org/ 10.1016/j.msea.2019.138209.
- [34] I. Bharti, N. Gupta, K. Gupta, Novel applications of functionally graded nano, optoelectronic and thermoelectric materials, Int. J. Mater. Mech. Manuf. 1 (3) (2013) 221–224, https://doi.org/10.7763/IJMMM.2013.V1.47.
- [35] P. Kumar, S.P. Harsha, Modal analysis of functionally graded piezoelectric material plates, Mater. Today. Proc. 28 (2020) 1481–1486, https://doi.org/10.1016/j. mater. 2020.04.825.
- [36] G.J. Snyder, E.S. Toberer, Complex thermoelectric materials, Nat. Mater. 7 (2) (2008) 105–114, https://doi.org/10.1038/nmat2090.
- [37] J. He, T.M. Tritt, Advances in thermoelectric materials research: Looking back and moving forward, Science. 357(6358) (2017) eaak9997, https://doi.org/10.1126/ science.aak9997.
- [38] F.J. DiSalvo, Thermoelectric cooling and power generation, Science 285 (5428) (1999) 703–706, https://doi.org/10.1126/science.285.5428.703.
- [39] I.T. Witting, T.C. Chasapis, F. Ricci, M. Peters, N.A. Heinz, G. Hautier, G.J. Snyder, The thermoelectric properties of bismuth telluride, Adv. Electron. Mater. 5 (6) (2019) 1800904, https://doi.org/10.1002/aelm.201800904.
- [40] K. Park, K. Ahn, J. Cha, S. Lee, S.I. Chae, S.-P. Cho, S. Ryee, J. Im, J. Lee, S.-D. Park, M.J. Han, I. Chung, T. Hyeon, Extraordinary off-stoichiometric bismuth telluride for enhanced n-type thermoelectric power factor, J. Am. Chem. Soc. 138 (43) (2016) 14458–14468, https://doi.org/10.1021/jacs.6b09222.
- [41] H.-L. Zhuang, H. Hu, J. Pei, B. Su, J.-W. Li, Y. Jiang, Z. Han, J.-F. Li, High ZT in p-type thermoelectric (Bi, Sb)₂Te₃ with built-in nanopores, Energy. Environ. Sci. 15 (5) (2022) 2039–2048, https://doi.org/10.1039/d2ee00119e.
- [42] W. Li, B. Poudel, A. Nozariasbmarz, R. Sriramdas, H. Zhu, H.B. Kang, S. Priya, Bismuth telluride/half-Heusler segmented thermoelectric unicouple modules provide 12% conversion efficiency, Adv. Energy. Mater. 10 (38) (2020) 2001924, https://doi.org/10.1002/aenm.202001924.
- [43] T. Ming, Y. Wu, C. Peng, Y. Tao, Thermal analysis on a segmented thermoelectric generator, Energy. 80 (2015) 388–399, https://doi.org/10.1016/j. energy 2014.11.080
- [44] Z. Ouyang, D. Li, Design of segmented high-performance thermoelectric generators with cost in consideration, Appl. Energy. 221 (2018) 112–121, https://doi.org/ 10.1016/j.apenergy.2018.03.106.
- [45] Z. He, M. Yang, Z. Wang, H. Chen, X. Zhang, Q. Jiang, V. Murugadoss, M. Huang, Z. Guo, H. Zhang, Optimization of segmented thermoelectric devices composed of high-temperature thermoelectric material La₂Te₃, Adv. Compos. Hybrid. Mater. 5 (4) (2022) 2884–2895, https://doi.org/10.1007/s42114-022-00471-w.
- [46] M. Aljaghtham, E. Celik, Design of cascade thermoelectric generation systems with improved thermal reliability, Energy. 243 (2022) 123032, https://doi.org/ 10.1016/j.energy.2021.123032.
- [47] G.J. Snyder, T.S. Ursell, Thermoelectric efficiency and compatibility, Phys. Rev. Lett. 91 (14) (2003) 148301, https://doi.org/10.1103/PhysRevLett.91.148301.
- [48] G.J. Snyder, Application of the compatibility factor to the design of segmented and cascaded thermoelectric generators, Appl. Phys. Lett. 84 (13) (2004) 2436–2438, https://doi.org/10.1063/1.1689396.
- [49] S.E. Yang, F. Kim, F. Ejaz, G.S. Lee, H. Ju, S. Choo, J. Lee, G. Kim, S.-H. Jung, S. Ahn, H.G. Chae, K.T. Kim, B. Kwon, J.S. Son, Composition-segmented BiSbTe thermoelectric generator fabricated by multimaterial 3D printing, Nano Energy. 81 (2021) 105638, https://doi.org/10.1016/j.nanoen.2020.105638.
- [50] Y. Huang, X. Shen, G. Wang, B. Zhang, S. Zheng, C.-C. Yang, X. Hu, S. Gong, G. Han, G. Wang, X. Lu, X. Zhou, High thermoelectric performance and compatibility in Cu₃SbSe₄-CuAlS₂ composites, Energy. Environ. Sci. 16 (4) (2023) 1763–1772, https://doi.org/10.1039/d3ee00128h.
- [51] D. Yang, X.L. Shi, M. Li, M. Nisar, A. Mansoor, S. Chen, Y. Chen, F. Li, H. Ma, G. X. Liang, X. Zhang, W. Liu, P. Fan, Z. Zheng, Z.G. Chen, Flexible power generators by Ag₂Se thin films with record-high thermoelectric performance, Nat. Commun. 15 (1) (2024) 923, https://doi.org/10.1038/s41467-024-45092-7.
- [52] C. Chi, G. Liu, M. An, Y. Zhang, D. Song, X. Qi, C. Zhao, Z. Wang, Y. Du, Z. Lin, Y. Lu, H. Huang, Y. Li, C. Lin, W. Ma, B. Huang, X. Du, X. Zhang, Reversible bipolar thermopower of ionic thermoelectric polymer composite for cyclic energy generation, Nat. Commun. 14 (1) (2023) 306, https://doi.org/10.1038/s41467-023-36018-w.
- [53] M.U. Muzaffar, B. Zhu, Q. Yang, Y. Zhou, S. Zhang, Z. Zhang, J. He, Suppressing bipolar effect to broadening the optimum range of thermoelectric performance for p-type bismuth telluride-based alloys via calcium doping, Mater. Today. Phys. 9 (2019), https://doi.org/10.1016/j.mtphys.2019.100130.
- [54] Z. Guo, K. Song, Z. Yan, P. Sun, X. Tan, G. Wu, Q. Zhang, G.-Q. Liu, B. Yu, J. Jiang, Broadening the optimum thermoelectric power generation range of p-type sintered Bi_{0.4}Sb_{1.6}Te₃ by suppressing bipolar effect, Chem. Eng. J. 426 (2021), https://doi. org/10.1016/j.cej.2021.131853.
- [55] M. Dariel, Z. Dashevsky, A. Jarashnely, S. Shusterman, A. Horowitz, Carrier concentration gradient generated in p-type PbTe crystals by unidirectional solidification, J. Cryst. Growth. 234 (1) (2002) 164–170, https://doi.org/10.1016/ S0022-0248(01)01660-8.

- [56] V. Kuznetsov, L. Kuznetsova, A. Kaliazin, D. Rowe, High performance functionally graded and segmented Bi₂Te₃-based materials for thermoelectric power generation, J. Mater. Sci. 37 (2002) 2893–2897, https://doi.org/10.1023/A: 1016.092224833
- [57] C.L. Cramer, J. Gonzalez-Julian, P.S. Colasuonno, T.B. Holland, Continuous functionally graded material to improve the thermoelectric properties of ZnO, J. Eur. Ceram. Soc. 37 (15) (2017) 4693–4700, https://doi.org/10.1016/j. jeurceramsoc.2017.07.019.
- [58] G. Guélou, C. Couder, C. Manière, C. Candolfi, B. Lenoir, L. Lallemant, C. Coureau, E. Guilmeau, Issues and opportunities from Peltier effect in functionally-graded colusites: From SPS temperature modeling to enhanced thermoelectric performances, Appl. Mater. Today. 22 (2021) 100948, https://doi.org/10.1016/j. apmt.2021.100948.
- [59] H.-Y. Pu, R.-Q. Xie, Y. Peng, Y. Yang, S.-Y. He, J. Luo, Y. Sun, S.-R. Xie, J. Luo, Accelerating sample preparation of graded thermoelectric materials using an automatic powder feeding system, Adv. Manuf. 7 (3) (2019) 278–287, https://doi. org/10.1007/s40436-019-00269-y.
- [60] W. Huang, X. Tan, J. Cai, S. Zhuang, C. Zhou, J. Wu, G. Liu, B. Liang, J. Jiang, Synergistic effects improve thermoelectric properties of zone-melted n-type Bi₂Te_{2.7}Se_{0.3}, Mater. Today. Phys. 32 (2023) 101022, https://doi.org/10.1016/j. mtphys.2023.101022.
- [61] L.Y. Lou, J. Yang, Y.K. Zhu, H. Liang, Y.X. Zhang, J. Feng, J. He, Z.H. Ge, L.D. Zhao, Tunable electrical conductivity and simultaneously enhanced thermoelectric and mechanical properties in n-type Bi₂Te₃, Adv. Sci. 9 (27) (2022) 2203250, https://doi.org/10.1002/advs.202203250
- [62] S. Byun, J. Cha, C. Zhou, Y.K. Lee, H. Lee, S.H. Park, W.B. Lee, I. Chung, Unusual n-type thermoelectric properties of Bi₂Te₃ doped with divalent alkali earth metals, J. Solid. State. Chem. 269 (2019) 396–400, https://doi.org/10.1016/j.ices.010.11016/j.
- [63] I.T. Witting, F. Ricci, T.C. Chasapis, G. Hautier, G.J. Snyder, The thermoelectric properties of n-Type bismuth telluride: bismuth selenide alloys Bi₂Te_{3-x}Se_x, Research. 2020 (2020) 4361703. https://doi.org/10.34133/2020/4361703.
- [64] A. Sahu, B. Russ, M. Liu, F. Yang, E.W. Zaia, M.P. Gordon, J.D. Forster, Y.Q. Zhang, M.C. Scott, K.A. Persson, N.E. Coates, R.A. Segalman, J.J. Urban, In-situ resonant band engineering of solution-processed semiconductors generates high performance n-type thermoelectric nano-inks, Nat. Commun. 11 (1) (2020) 2069, https://doi.org/10.1038/s41467-020-15933-2.
- [65] S. Wang, Y. Sun, J. Yang, B. Duan, L. Wu, W. Zhang, J. Yang, High thermoelectric performance in Te-free (Bi, Sb₂S_e3 via structural transition induced band convergence and chemical bond softening, Energy. Environ. Sci. 9 (11) (2016) 3436–3447, https://doi.org/10.1039/c6ee02674e.
- [66] C.L. Chen, T.H. Wang, Z.G. Yu, Y. Hutabalian, R.K. Vankayala, C.C. Chen, W.P. Hsieh, H.T. Jeng, D.H. Wei, Y.Y. Chen, Modulation doping enables ultrahigh power factor and thermoelectric ZT in n-type Bi₂Te_{2.7}Se_{0.3}, Adv. Sci. 9(20) (2022) 2201353, https://doi.org/10.1002/advs.202201353.
- [67] W.S. Liu, Q. Zhang, Y. Lan, S. Chen, X. Yan, Q. Zhang, H. Wang, D. Wang, G. Chen, Z. Ren, Thermoelectric property studies on Cu-doped n-type Cu_xBi₂Te_{2.7}Se_{0.3} nanocomposites, Adv. Energy. Mater. 1 (4) (2011) 577–587, https://doi.org/10.1002/aenm.201100149.
- [68] J.B. Vaney, S. Aminorroaya Yamini, H. Takaki, K. Kobayashi, N. Kobayashi, T. Mori, Magnetism-mediated thermoelectric performance of the Cr-doped bismuth telluride tetradymite, Mater. Today. Phys. 9 (2019) 100090, https://doi.org/10.1016/j.mtphys.2019.03.004.
- [69] W.-Y. Chen, X.-L. Shi, Q. Yang, M. Li, W. Lyu, T. Liu, T. Cao, B. Hu, W. Liu, S. Sun, Y. Mao, M. Dargusch, J. Zou, Z.-G. Chen, Solvothermally silver doping boosting the thermoelectric performance of polycrystalline Bi₂Te₃, Chem. Eng. J. 475 (2023) 146428, https://doi.org/10.1016/j.cej.2023.146428.
 [70] Y. Zhang, C. Xing, Y. Liu, M. Li, K. Xiao, P. Guardia, S. Lee, X. Han, A. Ostovari
- [70] Y. Zhang, C. Xing, Y. Liu, M. Li, K. Xiao, P. Guardia, S. Lee, X. Han, A. Ostovari Moghaddam, J. Josep Roa, J. Arbiol, M. Ibáñez, K. Pan, M. Prato, Y. Xie, A. Cabot, Influence of copper telluride nanodomains on the transport properties of n-type bismuth telluride, Chem. Eng. J. 418 (2021) 129374, https://doi.org/10.1016/j. cei.2021.129374.
- [71] J.S. Lee, A. Richardella, D.W. Rench, R.D. Fraleigh, T.C. Flanagan, J.A. Borchers, J. Tao, N. Samarth, Ferromagnetism and spin-dependent transport inn-type Mndoped bismuth telluride thin films, Phys. Rev. b. 89 (17) (2014) 174425, https:// doi.org/10.1103/PhysRevB.89.174425.
- [72] Z. Ouyang, D. Li, Modelling of segmented high-performance thermoelectric generators with effects of thermal radiation, electrical and thermal contact resistances, Sci. Rep. 6 (2016) 24123, https://doi.org/10.1038/srep24123.
- [73] Y. Zhou, X. Liu, B. Jia, T. Ding, D. Mao, T. Wang, G.W. Ho, J. He, Physics-guided co-designing flexible thermoelectrics with techno-economic sustainability for lowgraded heat harvesting, Sci. Adv. 9 (2023) eadf5701, https://doi.org/10.1126/ sciadv.adf5701.
- [74] Y. Lu, Y. Zhou, W. Wang, M. Hu, X. Huang, D. Mao, S. Huang, L. Xie, P. Lin, B. Jiang, B. Zhu, J. Feng, J. Shi, Q. Lou, Y. Huang, J. Yang, J. Li, G. Li, J. He, Staggered-layer-boosted flexible Bi₂Te₃ films with high thermoelectric performance, Nat. Nanotechnol. 18 (2023) 1281–1288, https://doi.org/10.1038/s41565-023-01457-5
- [75] L. Hu, T. Zhu, X. Liu, X. Zhao, Point Defect Engineering of High-Performance Bismuth-Telluride-Based Thermoelectric Materials, Adv. Funct. Mater. 24 (33) (2014) 5211–5218, https://doi.org/10.1002/adfm.201400474.
- [76] F. Kim, S.E. Yang, H. Ju, S. Choo, J. Lee, G. Kim, S.-H. Jung, S. Kim, C. Cha, K. T. Kim, S. Ahn, H.G. Chae, J.S. Son, Direct ink writing of three-dimensional thermoelectric microarchitectures, Nat. Electron. 4 (8) (2021) 579–587, https://doi.org/10.1038/s41928-021-00622-9.

- [77] C. Oztan, R. Welch, S. LeBlanc, Additive manufacturing of bulk thermoelectric Architectures: A Review, Energies. 15 (9) (2022), https://doi.org/10.3390/ epi5002121.
- [78] F. Kim, B. Kwon, Y. Eom, J.E. Lee, S. Park, S. Jo, S.H. Park, B.-S. Kim, H.J. Im, M. H. Lee, T.S. Min, K.T. Kim, H.G. Chae, W.P. King, J.S. Son, 3D printing of shape-conformable thermoelectric materials using all-inorganic Bi₂Te₃-based inks, Nat. Energy. 3 (4) (2018) 301–309, https://doi.org/10.1038/s41560-017-0071-2.
- [79] C. Dun, W. Kuang, N. Kempf, M. Saeidi-Javash, D.J. Singh, Y. Zhang, 3D printing of solution-processable 2D nanoplates and 1D nanorods for flexible thermoelectrics with ultrahigh power factor at low-medium temperatures, Adv. Sci. 6 (2019) 1901788, https://doi.org/10.1002/advs.201901788.
- [80] D. Zhang, X.J.G. Lim, X. Li, K. Saglik, S.F.D. Solco, X.Y. Tan, Y. Leow, W. Zhai, C.K. I. Tan, J. Xu, A. Suwardi, 3D-printed porous thermoelectrics for in situ energy harvesting, ACS Energy Lett. 8 (1) (2023) 332–338, https://doi.org/10.1021/acsenergylett.2c02425.
- [81] S.I. Kim, K.H. Lee, H.A. Mun, H.S. Kim, S.W. Hwang, J.W. Roh, D.J. Yang, W. H. Shin, X.S. Li, Y.H. Lee, G.J. Snyder, S.W. Kim, Dense dislocation arrays embedded in grain boundaries for high-performance bulk thermoelectrics, Science. 348 (6230) (2015) 109–114, https://doi.org/10.1126/science.aaa4166.

- [82] H. Goldsmid, J. Sharp, Estimation of the thermal band gap of a semiconductor from Seebeck measurements, J. Electron. Mater. 28 (1999) 869–872, https://doi.org/ 10.1007/s11664-999-0211-v.
- [83] M. Cutler, J.F. Leavy, R.L. Fitzpatrick, Electronic transport in semimetallic cerium sulfide, Phys Rev. 133 (1964) 4A, https://doi.org/10.1103/PhysRev.133.A1143.
- [84] A.-Y. Eum, S.-M. Choi, S. Lee, W.-S. Seo, J.-S. Park, S.-H. Yang, I.-H. Kim, Thermoelectric Properties of Bi₂Te_{3-y}Se_y: I_m Prepared by mechanical alloying and hot pressing, J. Electron. Mater. 46 (2017) 2623–2628, https://doi.org/10.1007/ s11664-016-4828-3.
- [85] Y.N. Nguyen, J. Park, S.H. Bae, D. Kim, K.Q. Dang, I. Son, Bulk Bi₂Te₃-based bendable thermoelectric device with highly elastic Cu-Be alloy foils, Mater. Today. Commun. 34 (2023) 105408, https://doi.org/10.1016/j.mtcomm.2023.105408.
- [86] X. Chen, F. Cai, R. Dong, X. Lei, R. Sui, L. Qiu, Z. Zeng, W. Sun, H. Zheng, Q. Zhang, Enhanced thermoelectric properties of n-type Bi₂Te_{2.7}Se_{0.3} for power generation, J. Mater. Sci. Mater. Electron. 31 (6) (2020) 4924–4930, https://doi.org/10.1007/ s10854-020-03057-8.
- [87] Z. Zhang, M. Sun, J. Liu, L. Cao, M. Su, Q. Liao, Y. Deng, L. Qin, Ultra-fast fabrication of Bi₂Te₃ based thermoelectric materials by flash-sintering at room temperature combining with spark plasma sintering, Sci. Rep. 12 (1) (2022) 10045, https://doi.org/10.1038/s41598-022-14405-5.